

A New Divergence Free Synthetic Eddy Method for the Reproduction of Inlet Flow Conditions for Embedded LES

R. Poletto · T. Craft · A. Revell

Received: date / Accepted: date

Abstract This paper describes a recent development of the Synthetic Eddy Method (SEM) proposed by Jarrin et al. (2009) for generation of synthetic turbulence. The present scheme is designed to produce a divergence-free turbulence field that can reproduce almost all possible states of Reynolds stress anisotropy. This improved representation, when used to provide inlet conditions for an LES, leads to reduced near-inlet pressure fluctuations in the LES and to a reduced development length requirement, both of which lead to lower computer resource requirements.

An advantage of this method with respect to forcing approaches (which require an iterative approach) is the suitability for direct usage with embedded LES. Results for a turbulent channel flow are reported here and compared to those from the original SEM, and other direct approaches such as the Vortex method of Sergent (2002) and the Synthesized Turbulence approach of Davidson and Billson (2006), showing overall improved performance and a more accurate representation of turbulence structures immediately downstream of the inlet.

1 Introduction

Large Eddy Simulation (LES) is gaining evermore industrial relevance due to increased computational capabilities and the ability to provide information about instantaneous fluctuations. Despite this, the definition of quality assurance measures required for industrial usage of LES remains a challenge (Celik et al., 2005). In contrast to Reynolds Averaged Navier-Stokes (RANS) methods LES may not obviously reach a grid independent solution and, arguably, the majority of practical LES studies can be considered to be ‘post-diction’ rather than prediction (which nevertheless provides a very useful tool for detailed flow analysis). Particularly for industrially relevant complex geometry, the computational requirements for what one could describe as ‘academically sound’ LES studies remain considerably high. As such there exists a substantial motivation to reduce the burden of such requirements by limiting the deployment of LES to those flow regions where one absolutely needs it, and applying a robust RANS approach in remaining parts of the domain. Such a methodology

School of Mechanical Aerospace and Civil Engineering, The University of Manchester, Manchester M13 9PL, UK

has been assigned the label of ‘Embedded LES’. In this framework two new problems are introduced; a method to move from RANS regions to LES and a second to return back from LES to RANS. The present paper deals with the former issue, where one must superimpose physically representative instantaneous turbulent fluctuations onto mean velocity profiles obtained by the RANS models at the interface of the two domains. An optimal synthetic turbulence algorithm to achieve this should have three main characteristics. First, it should require a minimal spatial development distance of the LES downstream of the interface, so that the dimensions of the LES region may be minimised. Secondly, it should require minimal computational effort compared to the resolution of the flow equations, so that the bottleneck is not with this algorithm. Thirdly, it should demonstrate satisfactory performance for input data coming from a range of RANS models. Given that the RANS model will generally be employed only in regions where one would expect good performance, it is reasonable to expect fairly reliable and realistic input data from it.

This problem is one that has been addressed by a range of different approaches, generally based on the superposition of realistic turbulent fluctuations upon a specified mean velocity profile. The main developments are summarised in the following section, but the reader is referred to Sagaut et al. (2006) and Tabor and Baba-Ahmadi (2010) for a more comprehensive review of the subject.

It is well known that simply imposing random fluctuations on top of a mean velocity field is insufficient, since a long development length is required before the flow reaches what might be considered to be a realistic turbulent state. In Lund et al. (1998) a first improvement to synthetic turbulence was suggested, by imposing a space correlation between the fluctuations; despite some improvement, shortfalls were still apparent as explained in Glaze and Frankel (2003). A further development was proposed by Sergent (2002), who used randomly generated concentrations of vorticity in the stream-wise direction to generate span-wise and wall-normal fluctuations. While this approach demonstrated significant improvement over the previous methods, it was essentially a two-dimensional method and suffered drawbacks from the requirement that stream-wise fluctuations were generated by an altogether separate equation, thereby being uncorrelated with the other components.

A different solution to the problem was suggested by Batten et al. (2004) and Davidson and Billson (2006) who imposed spectral distributions of the target fluctuations by a superposition of goniometric functions. In these approaches the spectral signature of the turbulence was essentially approximated by a modified von Kármán spectrum.

More recently, Jarrin et al. (2009) put forward a different approach to the problem where fluctuations are imposed by eddies convected through a virtual volume. This method was based on a three-dimensional correlation of fluctuations with a predefined shape function, and demonstrated an improved downstream development compared to other formulations; although recovery distance in a plane channel flow remained of the order of 10 half-channel heights. Subsequent work by Pamiès et al. (2009) demonstrated a substantial improvement over the original SEM by incorporating a more detailed definition of the eddy shape-function. In particular, multiple zones were defined in the near-wall region and the structure in each was adjusted to match well-documented observations of vorticity in the turbulent boundary layer. While the benefits of this approach are clear, some re-adjustment might become necessary for other flows.

The litterature invesrtigations performed showed that no method is able to describe a divergence free velocity field. This characteristic represents a lack in present synthetic turbulence as, even though the velocity is usually imposed on a 2D surface where, obviously, a divergence can not be defined since it is not possible to define a derivative in the surface-normal direction, all these methods imposes a net fluctuating mass flow at the inlet, superim-

posed on the bulk velocity which results in non physical pressure fluctuations. Furthermore synthetic turbulence, even when applied to 2D surfaces, implicitly defines the derivative in the surface normal direction via the time relation. If we consider a YZ plane where synthetic turbulence has to be applied, the following relation stands:

$$\frac{\partial u}{\partial t} = \frac{\partial u}{\partial x} u \quad (1)$$

This means that in every point of the 2D surface where synthetic turbulence is applied, the time derivative of the velocity is connected to the surface normal derivative via the velocity at that particular point. In a non divergence free method Equation (1) may be totally neglected, resulting in a missing relation between time and space derivatives. The divergence free method here suggested attempts to produce a velocity field where:

$$\frac{\partial u}{\partial t} = \frac{\partial u}{\partial x} U_b \quad (2)$$

which is an exemplification of the previous relation (where instantaneous velocity is substituted by the bulk velocity) but nevertheless it allows to firstly produce a relation between space and time derivatives, resulting in benefits of the downstream LES simulations.

2 The New Divergence Free SEM

2.1 Methodology

The present DFSEM is based on the methodology described in Jarrin et al. (2009) where synthetic eddies, each of which represents a set of velocity fluctuations, are convected through a box that entirely surrounds the inlet plane upon which a turbulent velocity field is required. These eddies, which are defined by their centre and a formulation for the velocity fluctuation distribution around it, are convected at each time step by the locally imposed mean velocity. Once they have traversed and exited the box they are regenerated at a random location on the box inlet plane. The number of eddies required for efficient performance of the algorithm is investigated in Section 3.

2.2 Divergence-Free Condition

The SEM proposed in Jarrin et al. (2009) defines velocity fluctuations according to the following:

$$u'_i(\mathbf{x}) = \frac{1}{\sqrt{N}} \sum_{k=1}^N a_{ij} \varepsilon_j^k f_\sigma \left(\frac{\mathbf{x} - \mathbf{x}^k}{\sigma} \right) \quad (3)$$

where N is the number of eddies introduced into the SEM domain, \mathbf{x}^k is the location of the centre of the k th eddy, σ^k is the turbulence length scale calculated at the eddy centre, $f_\sigma(\mathbf{x})$ is a suitable shape function, ε_j^k are random numbers with zero average and $\langle \varepsilon_j^k \varepsilon_j^k \rangle = 1$ which represent the eddies' intensities and a_{ij} are the Lund coefficients as defined in Lund et al. (1998) and reported by Equation (4). Although this formulation does allow any desired Reynolds stress field to be prescribed (via the a_{ij} coefficients), the velocity field will not, in general, also satisfy continuity.

$$a_{ij} = \begin{bmatrix} \sqrt{R_{11}} & 0 & 0 \\ \frac{R_{21}}{\frac{a_{11}}{a_{11}}} & \sqrt{R_{22} - a_{21}^2} & 0 \\ \frac{R_{31}}{a_{22}} & \frac{R_{32} - a_{22}a_{31}}{a_{22}} & \sqrt{R_{33} - a_{31}^2 - a_{32}^2} \end{bmatrix} \quad (4)$$

To obtain a divergence free method the original SEM is applied to the vorticity field which is then transformed back to the velocity field by taking the curl of it. In fact, vorticity and velocity fields are linked by Equation (5) in which, because of the hypothesis of incompressible flow, the second term on the right hand side vanishes leading to a poisson equation.

$$\nabla \times \omega' = \nabla(\nabla \cdot \mathbf{u}') - \nabla^2 \mathbf{u}' \quad (5)$$

The solution of this Poisson equation, achieved by using the Biot-Savart kernel, finally gives the fluctuating velocity field expressed as follows:

$$\mathbf{u}'(\mathbf{x}) = \sqrt{\frac{1}{N} \sum_{k=1}^N \frac{q_\sigma(|\mathbf{r}^k|)}{|\mathbf{r}^k|^3} \mathbf{r}^k \times \alpha^k} \quad (6)$$

where $\mathbf{r}^k = \frac{\mathbf{x} - \mathbf{x}^k}{\sigma^k}$, $q_\sigma(|\mathbf{r}|^k)$ is a suitable shape function and α_i^k are random numbers with zero average which represent the eddies' intensities. It is important to note here that Equation (6) is obtained from Equation (5) by imposing an isotropic length scale σ , which, as will be noted below, only allows the method to reproduce quasi-isotropic turbulence fluctuations.

2.3 Reproduction of Turbulence Anisotropy

In order to increase the turbulence anisotropy reproduction capabilities the present method employs a formulation similar to Equation (6), but defines a different length-scale, σ_i , in each of the coordinate directions x_i , and allows a different shape function to be associated with each direction. However, such a form no longer automatically satisfies the divergence-free condition ensured by Equation (6), and further constraints on the shape functions need to be considered in order to produce a divergence-free field. A convenient way of proceeding is to redefine the shape functions to be of the form $q_\sigma = q|\mathbf{r}^k|^3$ where q is a function which depends on the locations \mathbf{x} and \mathbf{x}^k , and \mathbf{r}^k differs slightly from its previous definition, as it now takes into account the length-scale anisotropy: $r_\beta^k = \frac{x_\beta - x_\beta^k}{\sigma_\beta^k}$. The new general formulation for the velocity fluctuations then becomes:

$$u'_\beta(\mathbf{x}) = \sqrt{\frac{1}{N} \sum_{k=1}^N q_\beta(\mathbf{x}, \mathbf{x}^k, \sigma^k) \varepsilon_{\beta jl} r_j^k \alpha_l^k} \quad (7)$$

In the above the cross product present in Equation (6) has been rewritten using the index notation for tensors, where ε_{ijl} is the Levi-Civita symbol, and no summation is implied over greek subscripts. As noted above, with the redefined shape functions the form of Equation (7) no longer automatically satisfies the divergence-free condition. However, on substituting it into the condition that $\nabla \cdot \mathbf{u}' = 0$, a sufficient condition for ensuring a divergence-free velocity field can be found to be to choose shape functions such that

$$r_2^k \frac{\partial q_1}{\partial x_1} = r_1^k \frac{\partial q_2}{\partial x_2} \quad r_3^k \frac{\partial q_2}{\partial x_2} = r_2^k \frac{\partial q_3}{\partial x_3} \quad r_3^k \frac{\partial q_1}{\partial x_1} = r_1^k \frac{\partial q_3}{\partial x_3} \quad (8)$$

A simple analytical function for q_i that satisfies the above restrictions is:

$$q_i = \begin{cases} \sigma_i [1 - (d^k)^2], & \text{if } d^k < 1 \\ 0, & \text{elsewhere} \end{cases} \quad (9)$$

where $d^k = \sqrt{(r_j^k)^2}$.

The function q_i chosen above is continuous everywhere, but its derivative is not strictly defined for $d^k = 1$, where it is only possible to define a right or left sided derivative. The above formulation thus defines a divergence-free velocity field everywhere except at the eddy surface ($d^k = 1$), although this formal omission is not believed to result in serious problems. The equation obtained by substituting Equation (9) into Equation (7) is here reported:

$$u'_\beta(\mathbf{x}) = \sqrt{\frac{1}{N}} \sum_{k=1}^N \sigma_\beta^k [1 - (d^k)^2] \varepsilon_{\beta jl} r_j^k \alpha_l^k \quad (10)$$

where the pedixes used in Equation (10) have the following meaning:

1. k represents the k -th eddy's dependent variables. Note that each eddy has mainly three variables that identifies it:
 - (a) centre location \mathbf{x}^k
 - (b) length scales σ^k
 - (c) intensity α^k
2. β represents the three different directions x, y and z
3. j and l are here to represent the cross product via the Levi-Civita symbol $\varepsilon_{\beta jl}$

Combining expressions for two fluctuating velocity components from Equation (10) and time-averaging leads to expressions for the Reynolds stresses, from which one can examine how the lengthscales, σ_i^k , and intensities, α_i^k , affect the stress anisotropy associated with the synthetically generated field given by Equation (11).

$$\langle u'_\beta u'_\gamma \rangle = \frac{1}{N} \sum_{k=1}^N \sigma_\beta^k \sigma_\gamma^k \varepsilon_{\beta jl} \varepsilon_{\gamma mn} \left\langle \left\{ [1 - (d^k)^2]^2 r_j^k r_m^k \right\} \right\rangle \langle (\alpha_l^k)(\alpha_n^k) \rangle \quad (11)$$

Equation (11) represents an important theoretical results because it shows that, since eddies are independent of each other, and the intensities are not correlated (so $\langle \alpha_l^k \alpha_m^k \rangle = 0$ for $l \neq m$), it is fairly straightforward to conclude that the predicted shear stresses ($\langle u'_\beta u'_\gamma \rangle$ for $\beta \neq \gamma$) will be zero. This problem can be circumvented by considering the above forms to be generating the stresses in the local principal axes coordinate system (where the Reynolds stress tensor is diagonal). Fluctuations in the global coordinate system are then generated by the following transformation of the velocity field:

$$u'_i^G(\mathbf{x}) = CR_{im}^{P \rightarrow G} u'_m^P \quad (12)$$

where $R_{im}^{P \rightarrow G}$ is the rotational transformation matrix from the principal to the global coordinate system, u'_m^P and u'_i^G are the velocity fluctuations in the principal axes and global systems respectively, and C is a normalization coefficient required in order to have $\langle u'_i^G \rangle = 1$ when $\langle (\alpha_l^k)^2 \rangle = 1$:

$$C = \frac{\sqrt{10V_0} \sum_{i=1}^3 \frac{\sigma_i}{3}}{\sqrt{N} \prod_{i=1}^3 \sigma_i} \min\{\sigma_i\} \quad (13)$$

where V_0 is the eddy box volume.

After examining how the prescribed lengthscales and intensities affect the Reynolds stresses of the resulting flowfield, a mapping approach has been chosen in order to reproduce virtually the whole Lumley triangle of possible Reynolds stress anisotropy states. It is found that for any choice of lengthscale ratios (σ_x/σ_y and σ_x/σ_z), varying the intensity α_l^k allows one to reproduce possible turbulence anisotropy states over a particular region of the triangle. The chosen points and the corresponding mapping areas used in the present work are displayed in Figure 1. The approach has been to define a series of ratios $\Gamma = \frac{\sigma_x}{\sigma_y} = \frac{\sigma_x}{\sigma_z}$ (effectively giving an elliptical shape to the eddies), corresponding to the regions shown in Figure 1. For a given Γ the Reynolds stresses are then reproduced by defining the following intensities:

$$\langle (\alpha_\beta^k)^2 \rangle = \frac{\lambda_j/\sigma_j^2 - 2\lambda_\beta/\sigma_\beta^2}{2\gamma} \quad (14)$$

where λ_i are the normal stresses in the local principal reference system and γ is a normalization coefficient obtained numerically and specified in Table 1. For any given Γ , it is possible to reproduce just a part of the triangle (since the right hand side of Equation (14) must be positive), and this is the reason for the sub-divisions shown in the Lumley triangle mapping. It can be noticed that with the series of ratios chosen in Table 1 most, but not quite all, of the Lumley triangle can be covered (the few remaining "gaps" could be covered by taking a larger set of ratios Γ , but for the present case only a few very near-wall locations fall into these 'gaps').

3 Sensitivity Study of Isolated Eddy Box

Preliminary tests were conducted in order to assess the sensitivity of the method to some of the input parameters of the DFSEM, mainly the number of eddies required to achieve satisfactory levels of averaged statistics. The model, as defined in the previous section, was implemented and applied to an inlet surface, of size $\delta \times \delta$, $\delta = 2 * \pi$, discretized by a grid of 128×128 nodes. The DFSEM is activated by imposing an isotropic state of turbulence and by assuming $U_b = 1$.

Tests have clearly demonstrated the impact of the factor $d = (\sigma_x \sigma_y \sigma_z N)/V_0$, which can be considered to represent the density of eddies imposed on the inlet plane. To illustrate this influence, results obtained for the streamwise velocity component u' at a particular spatial location are shown in Figure 3 for low ($d = 0.1$), medium ($d = 1$) and high ($d = 10$) densities. The first plot displays the time trace of the instantaneous velocity u' as eddies pass through this location in the eddy box. Non-zero values indicate the influence of one or more eddies as they pass through. While signals with medium and high eddy density return a picture which is qualitatively 'turbulent' in nature, the low density case, $d = 0.1$, gives a signal that appears to only pick up a single eddy at any given time, with frequent periods of zero activity indicating all eddies are outside the immediate vicinity of the sampling point.

The second plot in Figure 3 displays the computed values of the correlation $\langle u' u' \rangle$ as a function of the averaging time. As the computation progresses, this second moment should eventually return a value matching that of the imposed Reynolds stress. For the medium and high density cases, statistics are converged to within 10% of the final value after only a few hundred iterations, while for the lower eddy density of $d = 0.1$, noticeably more iterations are necessary. This behaviour can be elucidated further via a more detailed examination of the instantaneous synthetic turbulent velocity signal itself, and more specifically by plotting

the associated Probability Density Function (PDF), as in the last plot of Figure 3. As the eddy density is increased, a more complete PDF distribution is obtained.

Although the above results show the benefit of taking large values for d , the parameter is also significant from a computational point of view, since the computational effort (particularly memory requirement) increases proportionally to the number of eddies in the box at any one time. To demonstrate this point, the mean time per iteration is provided for computations performed with a range of eddy densities in Table 2.

Since, for practical purposes, one wants the computational cost of any synthetic turbulence methodology to be negligible compared to the overall simulation cost, the above results suggest, perhaps intuitively, that a sensible compromise is to take an eddy density of d close to the unity, which appears to give a good approximation of the velocity PDF with a relatively fast simulation time.

4 Channel Flow

4.1 Simulation Set Up

The new DFSEM, and other synthetic inlet methods, have been tested via application to inlet conditions for LES of a plane channel flow at $Re_\tau = 395$, for which reference DNS data is available from Moser et al. (1999). A domain of size $20\delta\pi \times 2\delta \times \pi\delta$, $\delta = 1$ has been used, with inlet conditions applied via the various synthetic turbulence methods tested and standard Neumann boundary conditions applied at the outlet. The performance of the inlet methods can be most efficiently assessed by comparing the development of flow conditions downstream of the inlet to those obtained from a periodic channel flow. To allow this comparison, a periodic LES has also been performed with an identical mesh and numerical parameters.

The computations have been performed using *Code-Saturne*, on a mesh of $500 \times 46 \times 82$ cells, giving a total of 188600 cells. These are arranged so that y^+ is around unity at the wall, and the non-dimensional grid-spacings in the stream-wise and span-wise directions are $\Delta x^+ = 50$ and $\Delta z^+ = 10$ respectively. A bulk velocity of $U_b/u_\tau = 17.55$ is imposed, via the inlet conditions, and the normalized time step used is $\Delta\tilde{t} = 0.07$ convective time units (CTU), where the latter is defined as $CTU = \delta/U_b$. The Courant number was kept below one at all times. Second order accurate time and spatial discretizations have been employed, and the standard Smagorinsky model adopted to account for the sub-grid-scale turbulence. The simulations have first been run for around 150 CTU, after which statistics have been collected over a further 1500 CTU. For activating synthetic turbulence DNS data from Moser et al. (1999) was used. Standard SEM has been simulated together with a modified version which takes into account of the mass flow rescaling as commented later and standard VORTEX (from Sergent (2002)) and DB (from Davidson and Billson (2006)).

4.2 Input Data and Length Scale Definition

For the tests reported here the DNS data of Moser et al. (1999) was used to provide Reynolds stress statistics for the DFSEM. These data are shown on the Lumley anisotropy triangle in Figure 4, where the grey area denotes the states that can be fully reproduced by the method as described above in Section 2. As can be seen, most of the DNS data points do indeed lie in this grey area, implying that the DFSEM should be capable of returning stresses close to

the desired levels. The few points lying outside the reproducible region are very close to the wall, mostly within the viscous sublayer, where turbulence levels are low, and the resultant errors in reproducing the turbulence anisotropy are not thought to be particularly serious.

Generally, in an Embedded LES framework, the Reynolds stresses for the DFSEM would come from a RANS model. Nevertheless, the present tests using full DNS statistics seem to be most appropriate in order to demonstrate the performance of the DFSEM, and its capability to make full use of anisotropic Reynolds stresses. Tests using data from a common RANS model, not reported here, have led to similar conclusions about the different inlet methods, and assessing the predictive accuracy of different RANS models is not the scope of the present work.

As described in Section 2.3, the present scheme sets the Reynolds stress anisotropy via the *ratios* of the different length scales σ_x , σ_y and σ_z , and their intensities $\langle(\alpha_i^k)^2\rangle$. The actual length scale magnitudes, here characterized by the average, $\sigma_{avg} = (\sigma_x + \sigma_y + \sigma_z)/3$, does not affect the Reynolds stress anisotropy in a homogeneous field, but does have some influence on the results in inhomogeneous situations, as will be seen below.

In the present work the average lengthscale, σ_{avg} , has been taken as

$$\sigma_{avg} = \min(k^{3/2}/\varepsilon, \kappa\delta, \max(\Delta x, \Delta y, \Delta z)) \quad (15)$$

where $k^{3/2}/\varepsilon$ is the local length scale provided by the DNS data (or would come from the RANS model in a typical embedded LES application), δ is the channel half-height, and κ the Von-Karman constant. The resulting Reynolds stress profiles generated by the DFSEM across the channel, compared to the DNS data, are shown in Figure 5. The comparison is generally very satisfactory, with most of the stress anisotropy being captured and, furthermore, the correlation between u' and v' being accurately reproduced. There is, however, a slight overestimate of the near-wall peak $\langle u' u' \rangle$ value, and a careful examination also shows that the stresses returned by the DFSEM do not quite go to zero at the wall surface.

The reason for the above discrepancies noted in Figure 5 lies, at least partly, in the role of the length scale prescription. Each eddy carries a certain set of velocity fluctuations across its entire volume, and its size, related to σ_{avg} , therefore determines the spatial extent over which these particular fluctuation levels are present as the eddy is convected across the inlet plane. In other words, the particular fluctuations associated with each eddy are seen not only on the trajectory of its centre, but also across a certain volume surrounding this, determined by the size of the eddy.

In order to visualize this behaviour, Figure 2 shows a representation of the eddies being convected through the inlet plane. The outlined rectangle represents the inlet surface and the ellipsoids are the eddies created by the DFSEM. As can be seen, the eddies are generally spherical towards the centre of the channel and elongated in the stream-wise direction as one approaches the wall. Different angles of inclination can also be seen, reflecting the changing direction of the Reynolds stress tensor principal axes. Each eddy carries velocity fluctuations which are applied across its whole volume, and hence contributes not only to the Reynolds stress levels on its centreline trajectory, but also to those in a certain area surrounding this. To characterise the effect of this non-local contribution of the eddies to the stress field one can examine the quantity F , defined at point \mathbf{P} by

$$F(\mathbf{P}) = \left| \frac{\partial \langle u'_i u'_j \rangle}{\partial y} \right| \cdot \frac{\sigma_{avg}}{u_\tau^2} \quad (16)$$

This expression can be interpreted as a non-dimensional measure of the local spatial gradient of $\langle u'_i u'_j \rangle$, with respect to the local σ_{avg} : a high value implies that the locally prescribed

length-scale will not be able to resolve fully the spatial variation of the Reynolds stress. Figure 6 shows the variation of F across the channel in the present case, with lengthscale σ_{avg} prescribed by Equation (15). As would be expected from Figure 5, the values of F associated with $\langle u'u' \rangle$ are highest, particularly close to the wall where $\langle u'u' \rangle$ changes rapidly. Nevertheless, over most of the channel the values of F are below 4, and the resulting stress profiles in Figure 5 suggest this is satisfactory.

4.3 Pressure Fluctuations and Bulk Mass Flow Correction

When employing a method such as the original SEM, which does not produce a divergence-free incoming velocity field, one might expect there to be locally high pressure fluctuations around the inlet, associated with the LES enforcing a divergence-free condition in the first cell of the computation. However, in initial tests of the present channel flow this effect was masked by another feature present in both the SEM and DFSEM (and potentially in other schemes) when applied to bounded internal flows. This feature arises since streamwise velocity fluctuations obtained from the formulations described in Section 2 can result in a non-constant bulk flow rate into the channel. Although each individual complete eddy has zero mass flow, there will commonly be instances where only part of an eddy is inside the domain, and a numerical sampling of a finite number of them may then return a non-zero mass flow rate associated with the fluctuating field. This has the effect of inducing a time-dependent bulk flow rate, and consequently a time-dependent pressure drop along the channel.

To illustrate the effect of the above problem, Figure 7 shows the levels of root mean squared (rms) pressure fluctuations along the channel for the SEM and the DFSEM (labelled as DFSEM_{nr} on the figure). In these calculations the fixed reference pressure is located at the channel exit, and consequently fluctuations in the bulk flow rate lead to fluctuations in pressure along the channel, and non-zero rms values, with the largest being at the inlet. The DFSEM does produce lower rms values compared to the original SEM, but they are still quite significant and substantial. To address the above problem, a bulk correction was applied to the inlet velocity profile by simply introducing a rescaling coefficient to ensure the total mass flow rate across the inlet plane remained constant. The line labelled DFSEM in Figure 7 shows the result of introducing this correction, and the fact that it almost entirely eliminates the corresponding pressure fluctuations.

Numerical simulations demonstrated that the above rescaling coefficient modified the velocity field by less than 1% in the channel flow, and so its effect on the divergence-free feature of the scheme was deemed negligible. A further benefit of the correction was that it significantly reduced the required computational time for the simulations, since the large pressure fluctuations along most of the channel length entailed additional iterations on the pressure-velocity coupling. Finally, it is reiterated that the need for rescaling is likely to be restricted to the case of wall-bounded internal flows, in which small mass-imbalances lead to a more pronounced effect on the pressure field than they would for non-bounded flows.

Once the above scaling algorithm has been applied to the schemes, the impact of the divergence-free condition on local pressure fluctuations near the inlet can be seen more clearly. Figure 8 shows iso-surfaces of rms pressure fluctuation levels close to the inlet along the centre of the channel for both SEM and DFSEM. As commented on above, in the simulations employing the SEM there are large pressure fluctuations immediately close to the inlet, where the LES has to rapidly adapt the incoming flow to give a divergence-free field in each computational cell. The DFSEM, on the other hand, results in much smaller

fluctuations and a more uniform rms distribution across this region of the channel, since the abrupt changes to enforce continuity are no longer needed.

5 Results

In the following, we report a detailed comparison of results from LES of a plane channel flow at $Re_\tau = 395$, in which inlet fluctuations are provided by the SEM of Jarrin et al. (2009), the method of Sergent (2002) (referred to as Vortex), the method of Davidson and Billson (2006) (referred to as DB) and the present version of the DFSEM described above.

Figure 9 presents the development of the wall skin-friction coefficient downstream of the inlet, located at $x/\delta = 0$. For reference, a periodic LES has been conducted on the same grid and the converged value of C_f is plotted together with lines indicating a 4% deviation from this value. When synthetic turbulence is applied at a flow inlet, there is typically a sudden drop of the friction coefficient immediately downstream, before recovery to the fully-developed value occurs further downstream. The distance required for this coefficient to return to its fully-developed value is defined as the development length. Clearly, the DB and Vortex schemes exhibit the most substantial drop-off from the inlet; both falling to around 55% of the periodic value. The improvement brought by considering 3D eddies is illustrated by the improved performance of the SEM and DFSEM, which drop to only around 85% and 96% of the periodic value respectively. In the case of the latter two approaches, this short fall-off is followed by a small over-shoot which slowly returns to the periodic solution over most of the remainder of the domain. In contrast, it is noted that the Vortex method predicts an evolution of C_f that returns more directly to the periodic LES signal, though it only approaches the LES value much further downstream than the SEM and DFSEM do, and does subsequently appear to drop slightly below the target value. The cause of the slight over-shoot of the velocity gradient in the case of the SEM and the DFSEM is yet to be fully identified, though one must point out the very near-wall nature of this quantity. Furthermore, in the context of an engineering model, it is very relevant to note that the DFSEM returns to a value within 4% of the periodic solution after only a very short development distance, and remains within this bound throughout the rest of the domain.

A deeper insight into the structure of the resolved turbulent flow in the interior of the domain is gleaned from Figures 10 and 11, by examining instantaneous values of vorticity. Contours of instantaneous ω_x are plotted at two planes parallel to the wall; Figure 10 displays the plane $y/\delta = 0.05$ (close to the wall) while Figure 11 displays the plane $y/\delta = 1$ (at the centre of the channel). In the near-wall region turbulence is known to develop into elongated stream-wise structures, which are clearly evident in the flow started with the SEM and DFSEM approaches in Figure 10. The flow initiated by the Vortex method indicates the correct qualitative behaviour, although the magnitude of the vorticity in this region is far lower than it should be, and does not deviate very much from zero within the region $x/\delta < 10$. The results from the DB approach indicate the presence of larger stream-wise structures, whose span-wise extent covers almost twice that of the correct dimensions, which are not recovered until around $x/\delta = 20$. Considering the flow near the channel centre, displayed in Figure 11, one may draw largely similar conclusions, although the performance of the Vortex method is noticeably improved. Indeed the more homogeneous, isotropic structure of turbulence in this region is perhaps more directly within the original philosophy of the Vortex method. Attention is drawn to the ability of the DFSEM to simultaneously achieve an accurate representation of the turbulent structures in both near-wall and channel centre

regions; testament to the ability of the scheme to reproduce turbulent fluctuation statistics across a range of Reynolds stress anisotropy levels.

In order to provide a more quantitative measure of the flow redevelopment, profiles of the Reynolds stress components have been extracted at selected locations downstream of the inlet and are presented in Figures 12, 13 and 14. Figure 12 shows the shear stress development, from which it is clear to see that the original SEM results in a sudden drop of correlation between u' and v' after the inlet, associated with the reduction in turbulent structures and drop in C_f seen above. This drop does not appear in the new DFSEM case, and the profiles rapidly converge towards the fully-developed one. A similar picture emerges for $\langle v'v' \rangle$ and $\langle u'u' \rangle$ in Figures 13 and 14. The initial reduction in $\langle v'v' \rangle$ associated with the SEM is perhaps not quite as severe as that seen in $\langle u'u' \rangle$. Nevertheless, because of the low level of turbulent correlations it still takes a significant distance to recover. The DFSEM approach again shows a much shorter recovery length, and for $\langle u'u' \rangle$ already returns very close to the fully-developed profile by $x/\delta \approx 3.6$.

6 Conclusions

A new synthetic turbulence generation method has been suggested as an improvement on the previous methodology of Jarrin et al. (2009). The new algorithm is able to impose a divergence free velocity field and to reproduce almost any possible state of Reynolds stress anisotropy. Results from a turbulent channel flow have demonstrated a general decrease in the required development region downstream of the inlet in a standard LES case: both the friction coefficient and the Reynolds stress profiles return to those obtained from a fully periodic computation in a shorter distance than that required by other methods tested.

The above results on reduced development length lead us to expect the method should result in significant computational savings when applied in fully embedded LES approaches, and further such tests are currently being carried out.

7 Acknowledgements

The authors gratefully acknowledge support from EDF (Électricité de France) under contract 4200071890, and compute time from EPSRC on the UK National HPC Facility, HECToR. Part of this work was carried out under the EU project ATAAC (Advanced Turbulence Simulation for Aerodynamic Application Challenges) funded by the European Community in the 7th Framework Programme under Contract No. ACP8-GA-2009-233710-ATAAC.

References

- P. Batten, U. Goldberg, and S. Chakravarthy. Interfacing statistical turbulence closures with Large-Eddy simulation. *AIAA Journal*, 42(3):485–492, 2004.
- I. Celik, Z. Cehreli, and I. Yavuz. Index of resolution quality for large eddy simulations. *Journal of fluids engineering*, 127(3):949–958, 2005.
- L. Davidson and M. Billson. Hybrid LES-RANS using synthesized turbulent fluctuations for forcing in the interface region. *International Journal of Heat and Fluid Flow*, 27(6):1028–1042, December 2006.

-
- D. Glaze and S. Frankel. Stochastic inlet conditions for Large-Eddy simulation of a fully turbulent jet. *AIAA Journal*, 41(6):1064–1073, 2003.
- N. Jarrin, R. Prosser, J.-C. Uribe, S. Benhamadouche, and D. Laurence. Reconstruction of turbulent fluctuations for hybrid RANS/LES simulations using a Synthetic-Eddy method. *International Journal of Heat and Fluid Flow*, 30(3):435–442, June 2009.
- T. Lund, X. Wu, and X. Squires. Generation of turbulent inflow data for Spatially-Developing boundary layer simulations. *Journal of Computational Physics*, 140(2):233–258, March 1998.
- R. Moser, J. Kim, and N. Mansour. Direct numerical simulation of turbulent channel flow up to $re_\tau = 590$. *Physics of Fluids*, 11(4):943–945, 1999.
- M. Pamiès, Pierre-Élie Weiss, Eric Garnier, Sébastien Deck, and Pierre Sagaut. Generation of synthetic turbulent inflow data for large eddy simulation of spatially evolving wall-bounded flows. *Physics of Fluids*, 21(4):045103, 2009.
- P Sagaut, S. Deck, and M. Terracol. *Multiscale and Multiresolution Approaches in Turbulence*. Imperial College press, 2006.
- M. E. Sergent. *Vers une Methodologie de Couplage Entre la Simulation des Grande Echelles et les Modeles Statistiques*. PhD thesis, Ecole Central de Lyon, 2002.
- G.R. Tabor and M.H. Baba-Ahmadi. Inlet conditions for large eddy simulation: A review. *Computers & Fluids*, 39(4):553–567, April 2010.

Γ	1	$\sqrt{2}$	$\sqrt{3}$	$\sqrt{4}$	$\sqrt{5}$	$\sqrt{6}$	$\sqrt{7}$	$\sqrt{8}$
γ	2.0	1.875	1.737	1.75	0.91	0.825	0.806	1.5

Table 1: Constant γ values used in the present work.

d [adim]	0.06	0.77	1.00	5.91
CPU time [s]	0.035	0.176	0.220	1.288

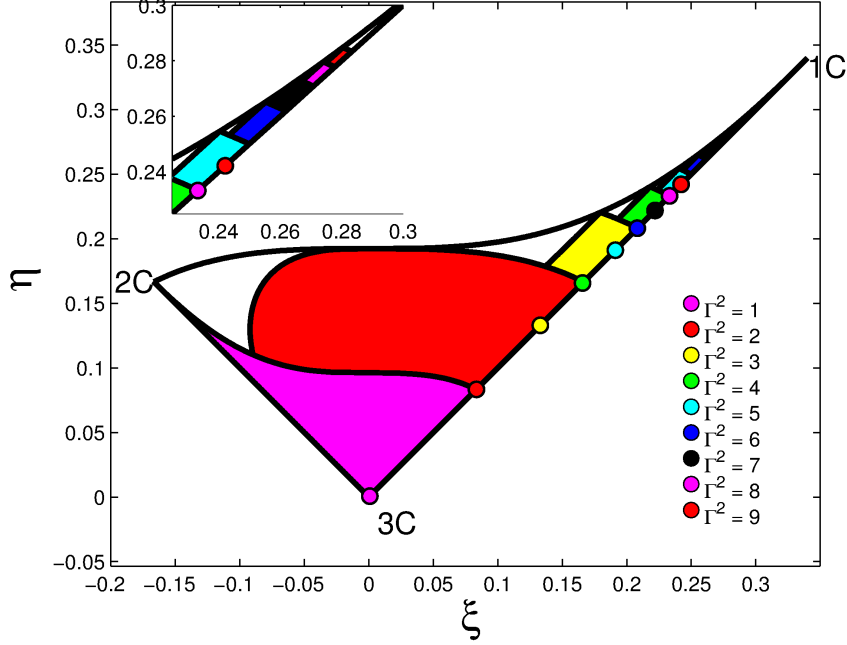
Table 2: DFSEM CPU time for a single time step at various d (performed on a 2MHz CPU)

Fig. 1: Lumley triangle mapped with the new DFSEM. $6\eta^2 = b_{ii}^2$, $6\xi^3 = b_{ii}^3$ and $b_{ij} = \frac{\langle u'_i u'_j \rangle}{\langle u'_k u'_k \rangle} - \frac{1}{3}\delta_{ij}$. Mapped regions are defined by the values of Γ given in Table 1.

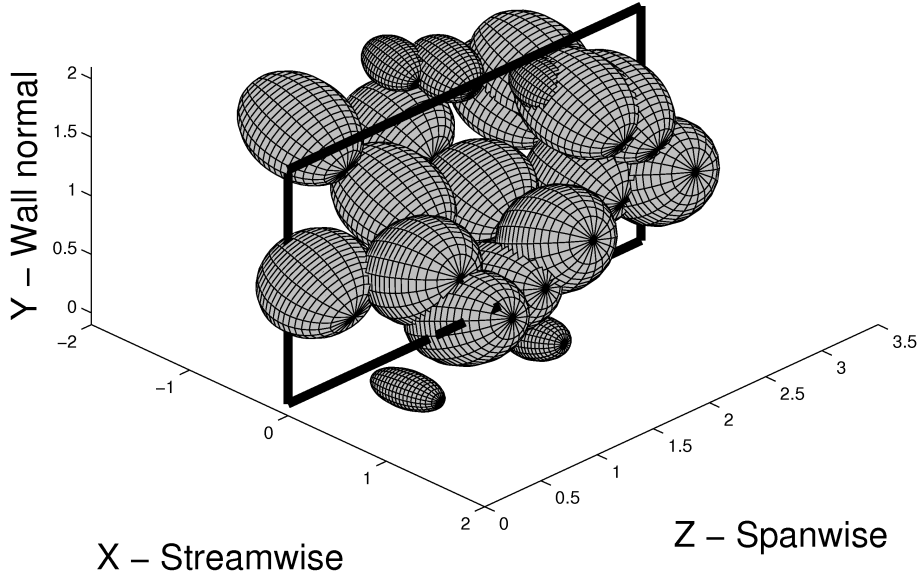


Fig. 2: Scheme of the eddies convected across the inlet plane by the DFSEM. Each spheroid represents the space zone affected by the perturbations given by a single eddy. These eddies are convected through an eddy box. The plane drawn represents the inlet surface of the LES simulation.

Fig. 3: Reproduction of an isotropic state of turbulence: influence of the eddy density d to the instantaneous velocity, to the convergence of $\langle u'_i u'_i \rangle$ and to the PDF.

Fig. 4: DNS data of $Re_\tau = 395$ channel flow from Moser et al. (1999), coloured by the local turbulent kinetic energy.

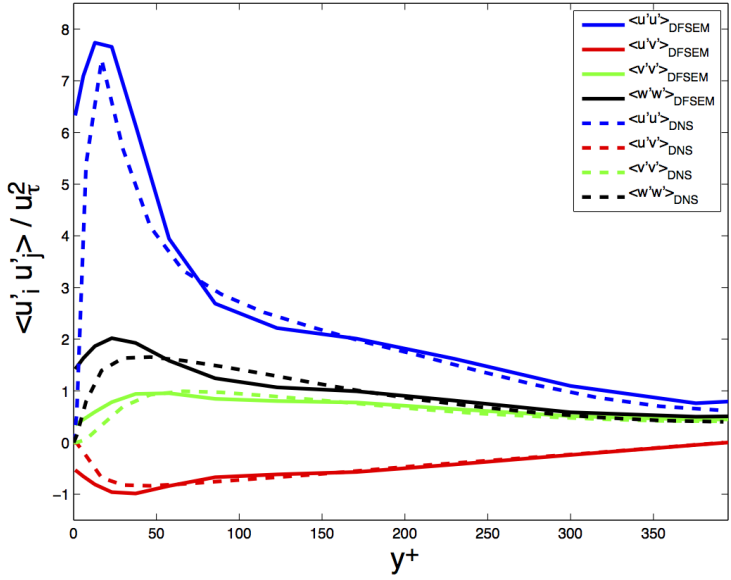


Fig. 5: Reproduced and prescribed Reynolds stresses. The DFSEM is not able to reproduce steep variations of stresses in the wall normal direction (see Figure 6). This is why close to the wall the reproduced stresses differ from the imposed ones. Note, in particular, that none of the stresses go to zero at the wall because of influence of nearby eddies.

Fig. 6: Parameter F evaluated for the test case considered, channel flow $Re_\tau = 395$. This parameter returns information about the capability of the DFSEM to reproduce a given Reynolds tensor distribution. In the zones where F is lower the DFSEM respects much more the imposed stresses, while where its values are higher there will be higher discrepancies.

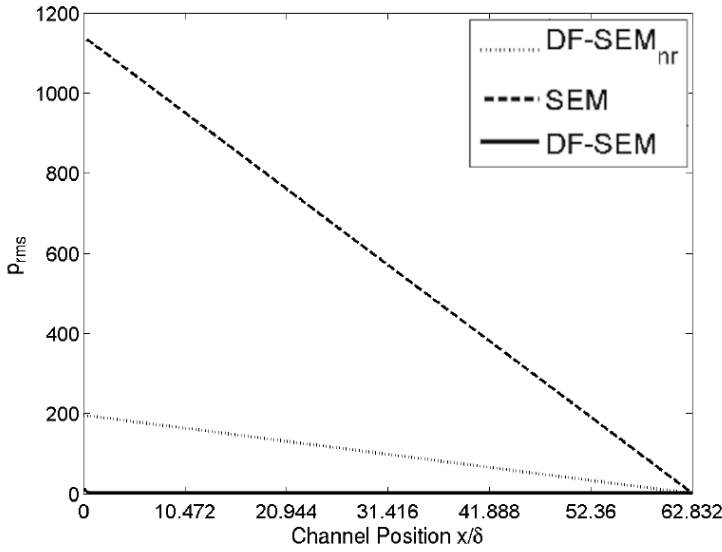


Fig. 7: Rms pressure fluctuations along the channel, using the original (unscaled) SEM and DFSEM (labelled as DFSEM_{nr}), and the DFSEM with velocity scaled to ensure a constant bulk flow rate.

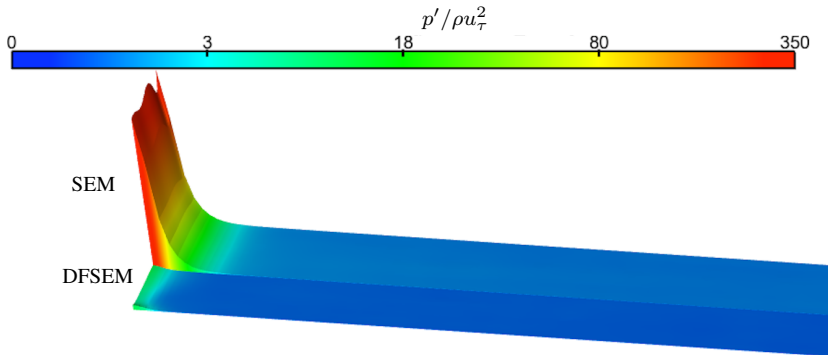


Fig. 8: RMS pressure fluctuations in the vicinity of the channel inlet with the SEM and the DFSEM. Both simulations take advantage of the flow rescaling in order to minimize the pressure fluctuations along the channel.

Fig. 9: C_f development along the channel; comparison of different inlet schemes against periodic solution. The DFSEM is compared against original SEM (reported as SEMnj) and some improvements: anisotropic SEM (SEMany) and SEM with rescaled mass flow (SEMresc). VORTEX and Davidson's (DB) methodologies are reported as well.

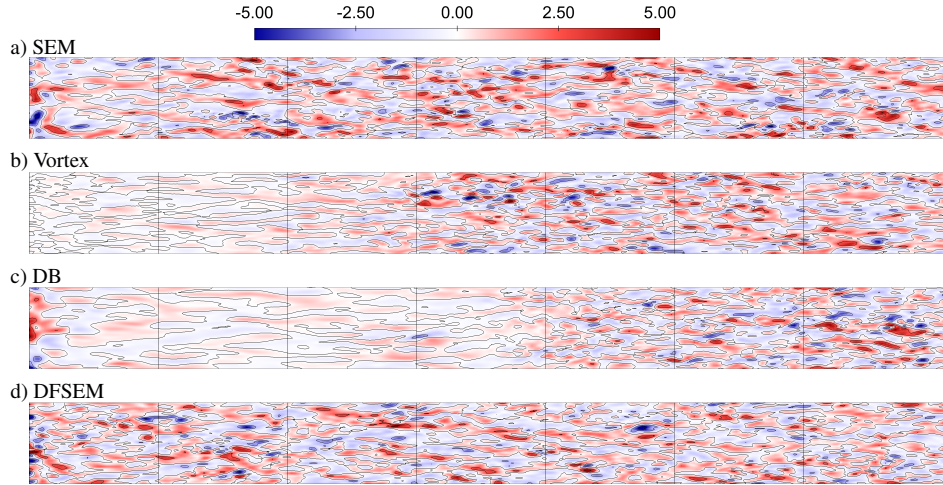


Fig. 10: Contours of stream-wise component of instantaneous vorticity, ω_x , over the XZ plane at $y/\delta = 0.05$. Flow left to right; where vertical black lines denote stream wise intervals of 5δ .

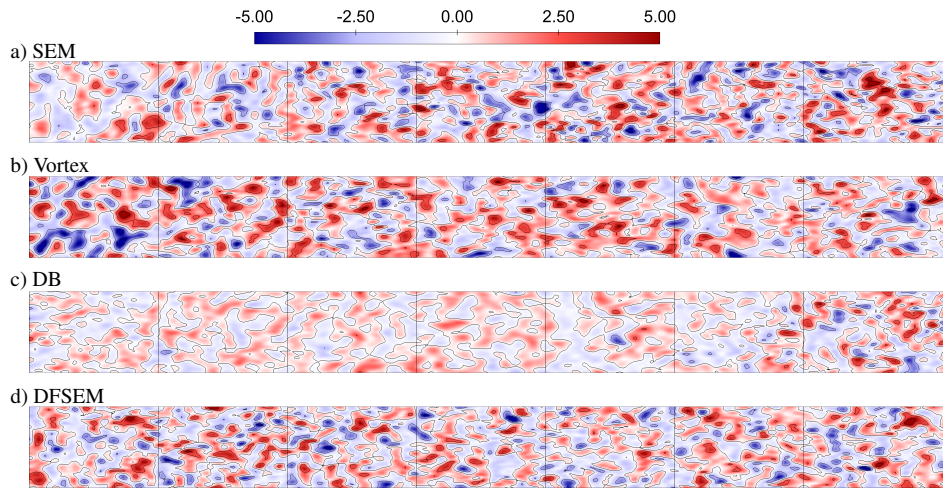


Fig. 11: Comparison of stream-wise component of instantaneous vorticity, ω_x , over the XZ planes at $y/\delta = 1$. Flow left to right; where vertical black lines denote stream wise intervals of 5δ .

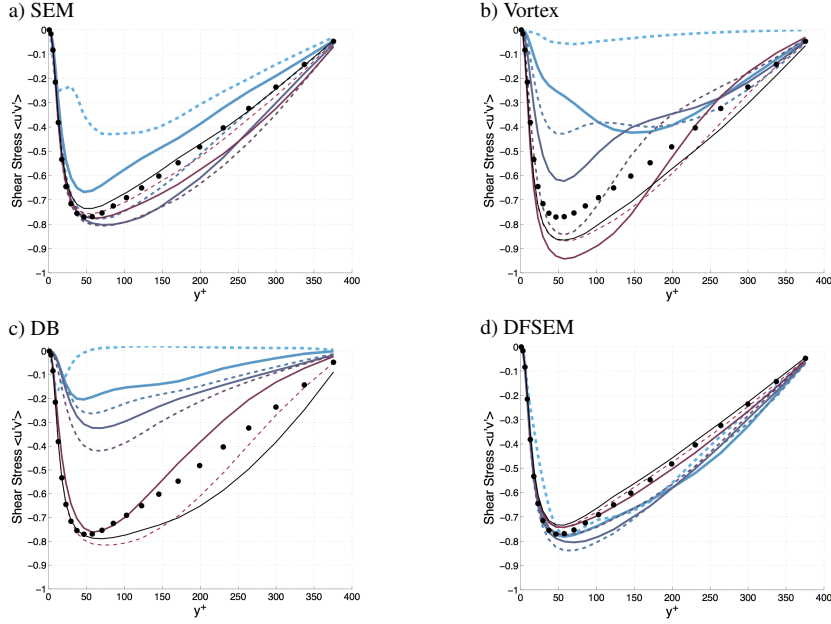


Fig. 12: $\langle u'v' \rangle$ profiles at selected stream-wise locations using various inlet conditions.

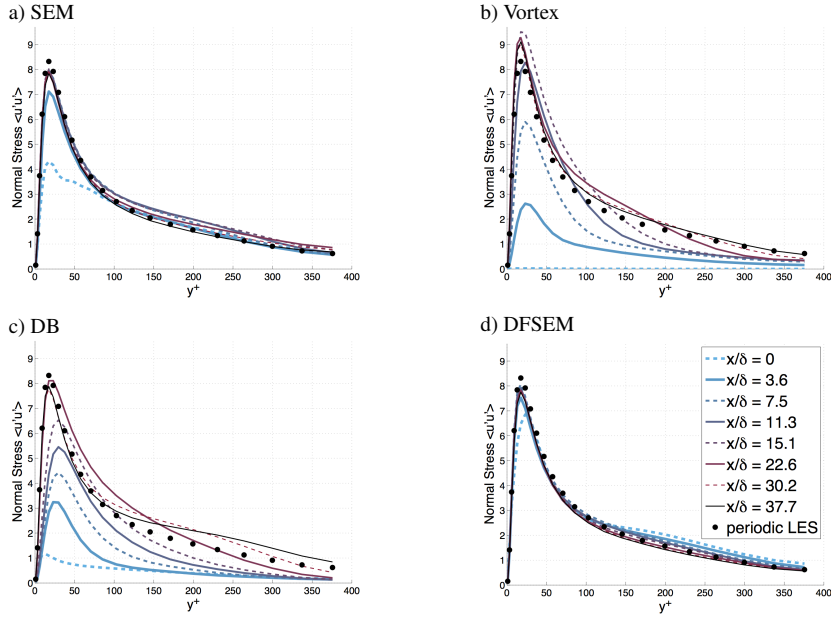


Fig. 13: $\langle u'u' \rangle$ profiles at selected stream-wise locations using various inlet conditions.

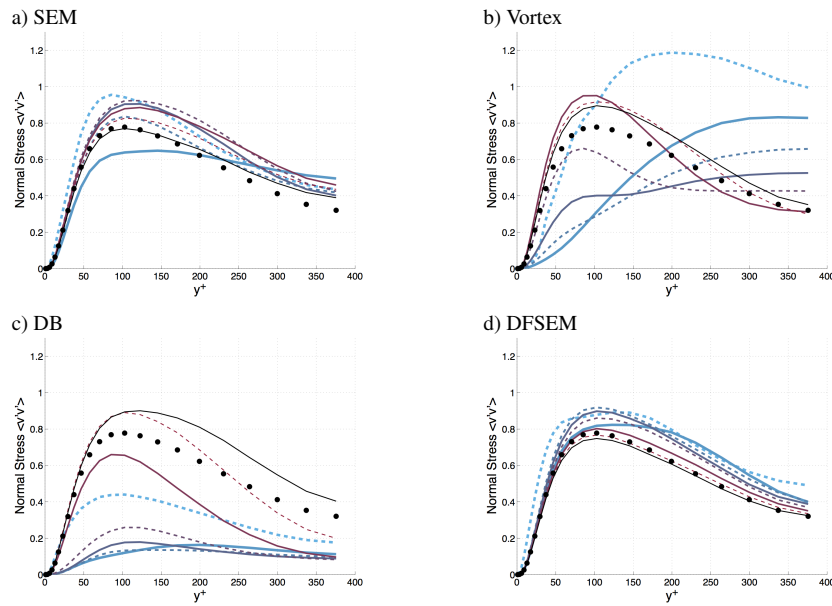


Fig. 14: $\langle v'v' \rangle$ profiles at selected stream-wise locations using various inlet conditions.